Advanced Functional Materials

ADVANCED FUNCTIONAL MATERIALS
www.afm-journal.de

RESEARCH ARTICLE

MMP-2/Temperature Dual-Responsive Smart Eutectogels With Strong Tissue Adhesion, Superior Stability, and Adaptability for Glaucoma Treatment

Yaozhi Zhang[1] | Menglu Jiang[2] | Shiqi Zhang[2] | Aimeng Dong[2] | Fenghua Zhang[1] | Yanju Liu[3] | Huiping Yuan[2] | Jinsong Leng[1]

[1]Centre For Composite Materials and Structures, Harbin Institute of Technology (HIT), Harbin, P. R. China | [2]Department of Ophthalmology, The Future Medicine Laboratory, The Second Affiliated Hospital of Harbin Medical University, Harbin, P. R. China | [3]Department of Astronautical Science and Mechanics, Harbin Institute of Technology (HIT), Harbin, P. R. China

Correspondence: Fenghua Zhang (zhangfenghua@hit.edu.cn) | Huiping Yuan (600761@hrbmu.edu.cn) | Jinsong Leng (lengjs@hit.edu.cn)

Received: 28 January 2026 | **Revised:** 23 May 2026 | **Accepted:** 2 June 2026

Keywords: 4D printing | drug delivery | glaucoma treatment | smart eutectogels | stimuli-responsiveness

ABSTRACT

Traditional hydrogel-based drug delivery systems face critical limitations, including poor toughness and adhesion, and low drug utilization efficiency, which collectively limit their efficacy in glaucoma treatment. Deep eutectic solvents (DESs) can effectively address these limitations because they are structurally tunable and exhibit high rates of drug dissolution. Herein, we apply β-cyclodextrin and phytic acid to prepare a novel DES, which was used to fabricate a deep eutectic smart gel drug delivery system (DSGS). The DES establish multi-hydrogen-bonded shielding networks with polymer chains, endowing the DSGS with an ocular tissue-matched modulus and a high toughness of 5.94 MJ·m^{-3}. Notably, the DSGS enables precise drug release in response to dual stimuli: matrix metalloproteinase-2 and temperature. We employ 4D printing technology to engineer a novel glaucoma drainage device (GDD) from the DSGS loaded with an antifibrotic drug for glaucoma treatment. Based on the synergistic effect of DSGS and the drug, the GDD regulates intraocular pressure (IOP), suppresses fibrosis, and restructures the extracellular matrix collagen architecture in vivo. Furthermore, the DSGS is injectable and exhibits strong tissue adhesion. Following minimally invasive implantation into the conjunctiva, a stable IOP was maintained for 30 days. This innovative design represents a promising direction for future drug delivery.

1 | Introduction

Glaucoma is the second leading cause of blindness worldwide, and severely threatens vision and quality of life [1]. Lowering intraocular pressure (IOP) is critical for managing glaucoma [2]. When maximally tolerated medication or laser therapy fails, the implantation of glaucoma drainage devices (GDDs) becomes the primary surgical option for severe and refractory glaucoma [3]. Unfortunately, the silicone implants commonly used in clinical practice often trigger abnormal wound-healing responses, leading to scar-tissue formation [4]. Scar tissue can obstruct the surgically created aqueous humor outflow pathway, leading to a gradual loss of IOP control and ultimately surgical failure [5].

Postoperative fibrosis following GDD implantation is associated with excessive inflammation [5]. In particular, the C–C

Yaozhi Zhang and Menglu Jiang contributed equally to this work.

motif chemokine ligand 2 – C–C chemokine receptor 2 (CCL2–CCR2) signaling axis mediates monocyte recruitment and M1 macrophage polarization, amplifying early inflammatory responses, and promoting fibroblast proliferation and extracellular matrix deposition [6]. Therefore, targeting the CCL2–CCR2 axis to suppress M1 polarization while promoting M2-dominant macrophage responses represents a promising strategy for modulating the inflammatory microenvironment and reducing scar formation.

Compared to the direct administration of drugs to block the CCL2–CCR2 axis, hydrogel-based drug delivery systems offer significant advantages [7–9]. These systems utilize the 3D network structure to load drugs, enabling sustained and targeted release through hydrogel degradation or in response to stimuli [7, 10, 11]. However, the mechanical properties of these hydrogels are often difficult to optimize, resulting in low toughness and adhesion, making them prone to damage and detachment during use [12], which limits their long-term stability. Furthermore, the drug-loading capacity and controlled release of these hydrogels were suboptimal. In particular, the release of certain drugs may be too rapid or unstable, compromising therapeutic efficacy. Enhancing hydrogel stability and improving drug release profiles are key challenges faced by researchers.

Deep eutectic gels, also known as eutectogels, have emerged as promising alternatives to overcome the limitations of traditional hydrogels. Eutectogels composed of structurally tunable deep eutectic solvents (DESs) can be rationally designed to enhance drug solubility and delivery-system stability [13–16]. Recently, researchers have attempted to incorporate supramolecular hosts and functional polymers into eutectogel systems to expand their functionalities in drug delivery. Denora et al. [17]. found that β-cyclodextrin-based DESs could synergistically enhance the drug loading capacity, stability, and controlled release ability. At the same time, Zhang et al. [18]. demonstrated that poly (N-acryloyl glycinamide) (PNAGA), a polymer containing multiple hydrogen-bonding structures, could form a physically crosslinked network in DES, endowing the gel with mechanical strength, temperature responsiveness, and thermal stability.

Furthermore, conferring matrix metalloproteinase-2 (MMP-2) responsiveness to the eutectogels is crucial for their biomedical applications. This strategy stems from a key pathological observation that tissue inflammation leads to the specific upregulation of MMP-2 [19, 20]. This pathological signature can be harnessed as a switch for intelligent drug release, enabling precise drug delivery at the disease site to enhance therapeutic efficacy while reducing systemic side effects.

Herein, we innovatively employed β-cyclodextrin (CD) and phytic acid (PA) to synthesize the DES, into which N-acryloyl glycinamide (NAGA) and gelatin were incorporated to form a precursor. The photopolymerization of NAGA within the precursor yielded PNAGA, which subsequently underwent spontaneous hydrogen-bond-mediated crosslinking to form a deep eutectic smart gel drug delivery system (DSGS). Specifically, CD enhances the drug solubility, PA forms abundant secondary dynamic reversible hydrogen bonds with the PNAGA chains, resulting in multiple hydrogen-bonded shielding networks (Figure 1a). This structure endows the DSGS with tunable mechanical properties, strong tissue adhesion, and temperature responsiveness. The incorporation of gelatin, which exhibits unique MMP-2-responsive degradation, enables the DSGS to respond to the presence of MMP-2. The dual responsiveness to temperature and MMP-2 enables the DSGS to intelligently regulate the drug-release rate.

For glaucoma patients requiring surgical intervention, a novel GDD integrating DSGS with a CCR2 inhibitor (DSGS-C) was fabricated using 4D printing technology (3D printing based on smart materials). This technique enables the precise fabrication of complex structures and endows the GDD with stimuli-responsive drug release capability. The results demonstrated that the GDD exhibited excellent therapeutic efficacy for glaucoma. This effect is attributed to the synergistic action of DSGS and the CCR2 inhibitor. DSGS inhibited M1 macrophage polarization, thereby exerting anti-inflammatory effects. In addition, the CCR2 inhibitor released from DSGS blocks the interaction between CCL2 and its primary receptor, CCR2, reducing macrophage recruitment and polarization, preventing fibroblast proliferation, and consequently suppressing scar formation (Figure 1b). Furthermore, for mild glaucoma, DSGS loaded with timolol maleate (DSGS-T), injected into the conjunctival space, maintains a stable IOP for 30 days via sustained drug release.

2 | Results and Discussion

2.1 | Mechanism of DES and DSGS Performance

To address the clinical challenges of transiently high drug concentrations and uncontrolled drug release commonly exhibited by current glaucoma treatments, we designed a novel DES for application in a DSGS. First, a series of DESs was synthesized using PA as the hydrogen-bond donor and CD as the hydrogen-bond acceptor at mass ratios of 1:1, 2:1, 3:1, 4:1, 5:1, and 6:1. DES formation was observed for all mass ratios of PA to CD except 1:1, and the resulting DESs appeared as a yellow liquid (Figures S1 and S2). The DESs formed at PA-to-CD mass ratios of 2:1, 3:1, 4:1, 5:1, and 6:1 was named DES-1, DES-2, DES-3, DES-4, and DES-5, respectively. CD is a cyclic oligosaccharide that can be absorbed by humans. Additionally, the internal truncated cone-shaped cavities of CD can encapsulate various drugs, improving their solubility and bioavailability [21]. PA, an organophosphorus compound extracted from plant seeds, contains six phosphate groups that provide multiple hydrogen bonding sites for CD (Figure 2a). The weak acidity of PA inhibits bacterial growth and exerts anti-inflammatory effects [22]. The viscosity of the DESs was tested using a viscometer. As shown in Figure S3, the higher the PA content in the DES, the lower the viscosity. Furthermore, the viscosity of the DESs decreased with an increase in temperature. Additionally, rheological testing of the DESs indicated shear-thinning behavior (Figure S4). As the shear rate increased, the viscosity of the DESs initially dropped significantly and then remained stable.

The ^{1}H nuclear magnetic resonance (^{1}H NMR) spectra in Figure 2b show that for all DESs, the CD and PA peaks exhibit blue shifts owing to hydrogen bonding [23]. Furthermore, no new absorption peaks are observed for the DESs, indicating that no new chemical bonds were formed during synthesis. The X-ray

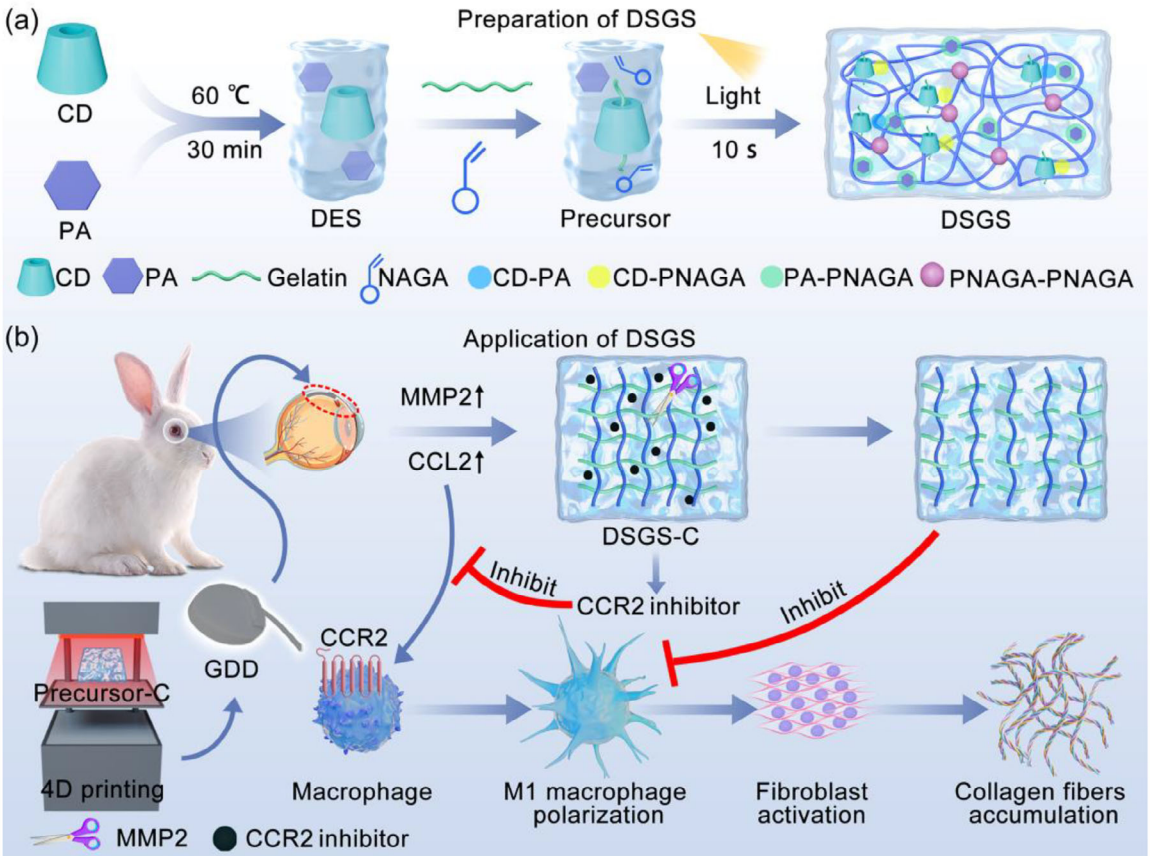

FIGURE 1 | Schematic of the design and application of DSGS.

diffraction (XRD) patterns in Figure 2c show broad diffraction peaks at 50°, indicating the presence of PA with an amorphous structure. The characteristic peaks of CD are sharp, indicative of a highly crystalline material [22]. During the formation of the DESs, hydrogen bonds are formed between CD and PA, resulting in an amorphous material, confirmed by the disappearance of the sharp peaks in the CD spectrum.

The thermal properties of the DESs were investigated using differential scanning calorimetry (DSC). The results (Figure 2d) show that the standard melting point (T_m) of pure CD is 334°C. With the addition of PA, only the glass transition temperature (T_g) was observed in the DSC curves of the DESs at lower temperatures. Furthermore, as the PA content increased, the T_g gradually decreased, reaching a minimum of −10.8°C. The results indicate that the DESs formed by the mixture of CD and PA can maintain an amorphous phase over a wide temperature range [24].

Subsequently, NAGA and gelatin were introduced into different DESs. Under ultraviolet (UV; 405 nm) irradiation, the photoinitiator (lithium phenyl-2,4,6-trimethylbenzoylphosphinate ; LAP) was activated to generate free radicals [25], initiating the rapid photopolymerization of NAGA and the formation of DSGSs. The name of the DSGS corresponds to that of its respective DES. The X-ray photoelectron spectroscopy (XPS) spectra provide in-depth insights into the composition of the DSGS materials. The high-resolution XPS C1s spectrum (Figure 2e) exhibits characteristic peaks at 284.6 eV (C—C), 285.0 eV (C—O; C—N), 285.0 eV (C═O), and 288.7 eV (O—C═O from gelatin). The corresponding O1s peaks (Figure S5) are observed at 532.1 eV (C—O) and 532.7 eV (C═O). The results show that DSGS retains a rich presence of oxygen-containing functional groups, providing a structural basis for hydrogen bonding interactions. On the other hand, all the peak positions are consistent with the expected binding energies of the functional groups in the physically mixed components, with no new peaks or significant shifts in binding energies characteristic of covalent crosslinking. This further confirms that the supramolecular gel is successfully formed through non-covalent intermolecular interactions [26].

Using DSGS-1 as an example, the real-time gelation process was monitored using a photorheometer with a customized optical setup (Figure S6). As shown in Figure 2f, before UV exposure, the storage modulus (G′) of DSGS is lower than its loss modulus (G″), indicating that the precursor exhibits a fluid state. This indicates that the hydrogen bond cross-linking network generated by gelatin is insufficient to form a 3D network in the precursor [27]. Upon UV irradiation, both G′ and G″ increase rapidly, and after 10 s, G′ exceeds G″, representing a transition from a fluid state to one dominated by elastic behavior [28]. This confirms the formation of the gel, which exhibits stable performance after 2 min of UV irradiation. Figure 2g shows a photograph of the transformation of the precursor into a gel. The comparison before and after UV exposure confirms that gel formation was due to hydrogen bond cross-linking generated after the photopolymerization of NAGA, rather than the effect of gelatin. Therefore, the key to understanding the formation

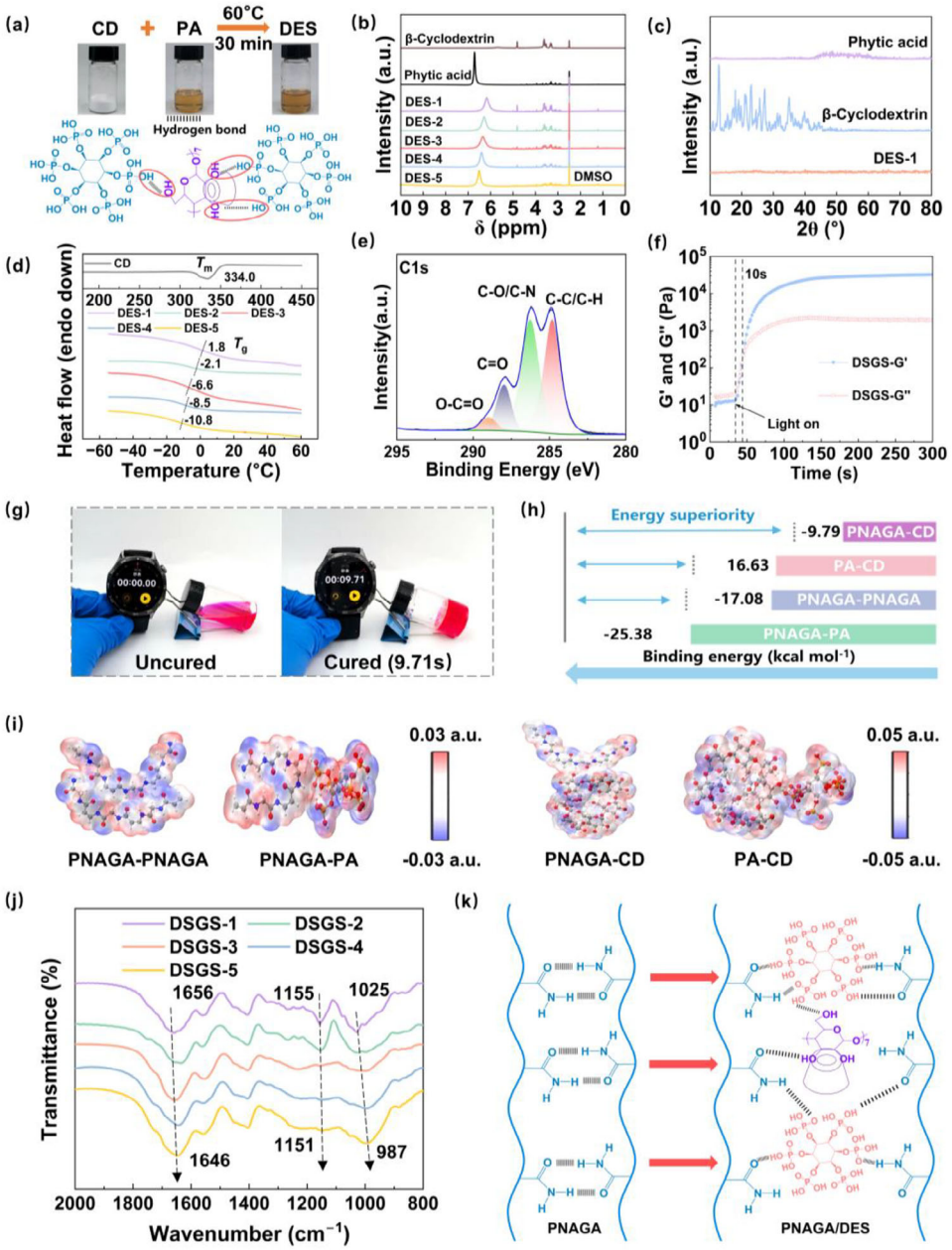

FIGURE 2 | Preparation and establishment mechanism of DESs and DSGSs. (a) Preparation method of DES using CD and PA. (b) ^{1}H NMR spectra of CD, PA, and the DESs. (c) XRD patterns of PA, CD, and DES-1. (d) DSC curves of CD and DESs. (e) XPS C1s spectrum of DSGS. (f) Real-time modulus changes of DSGS under UV light. (g) Demonstration of rapid gelation of DSGS. (h) Binding energy values for component pairs in DSGS. (i) Molecular electrostatic potential surfaces of PNAGA-PNAGA, PNAGA-PA, PNAGA-CD, and PA-CD blended systems. (j) FT-IR spectra of DSGSs. (k) Possible interaction mechanisms between DES and PNAGA polymer chains within DSGS.

mechanism of DSGS lies in elucidating the influence of DES on the PNAGA polymer segments.

The hydrogen bonds between the DES and PNAGA chains were investigated using density functional theory (DFT) calculations (Table S1) to provide a preliminary understanding of the role of DES in the formation of the polymer networks. As shown in Figure 2h, the PA-PNAGA pair exhibits an energy advantage over the other component pairs within the DSGS polymer network. Furthermore, the carbonyl groups present in PNAGA show a preference for binding to the hydrogen bonding sites of PA rather than forming interactions within the PNAGA chain itself (Figure 2i). Fourier transform infrared (FT-IR) spectra of the DSGSs show that as the PA content increases, the characteristic absorption peak of the —P—OH bonds shifts from 1025 to 987 cm^{-1}, while the characteristic absorption peak of the —P═O bonds shifts from 1155 to 1151 cm^{-1} (Figure 2j). These significant shifts to lower wavenumbers indicate the formation of strong hydrogen bonds owing to the incorporation of PA [29]. Additionally, the intensity of the characteristic absorption peak of PNAGA attributed to —C═O bonds remain largely unchanged, but the peak shifts to higher binding energy, suggesting that CD does not break the hydrogen bonds between PNAGA and PA. Overall, the PA molecules are incorporated into the PNAGA

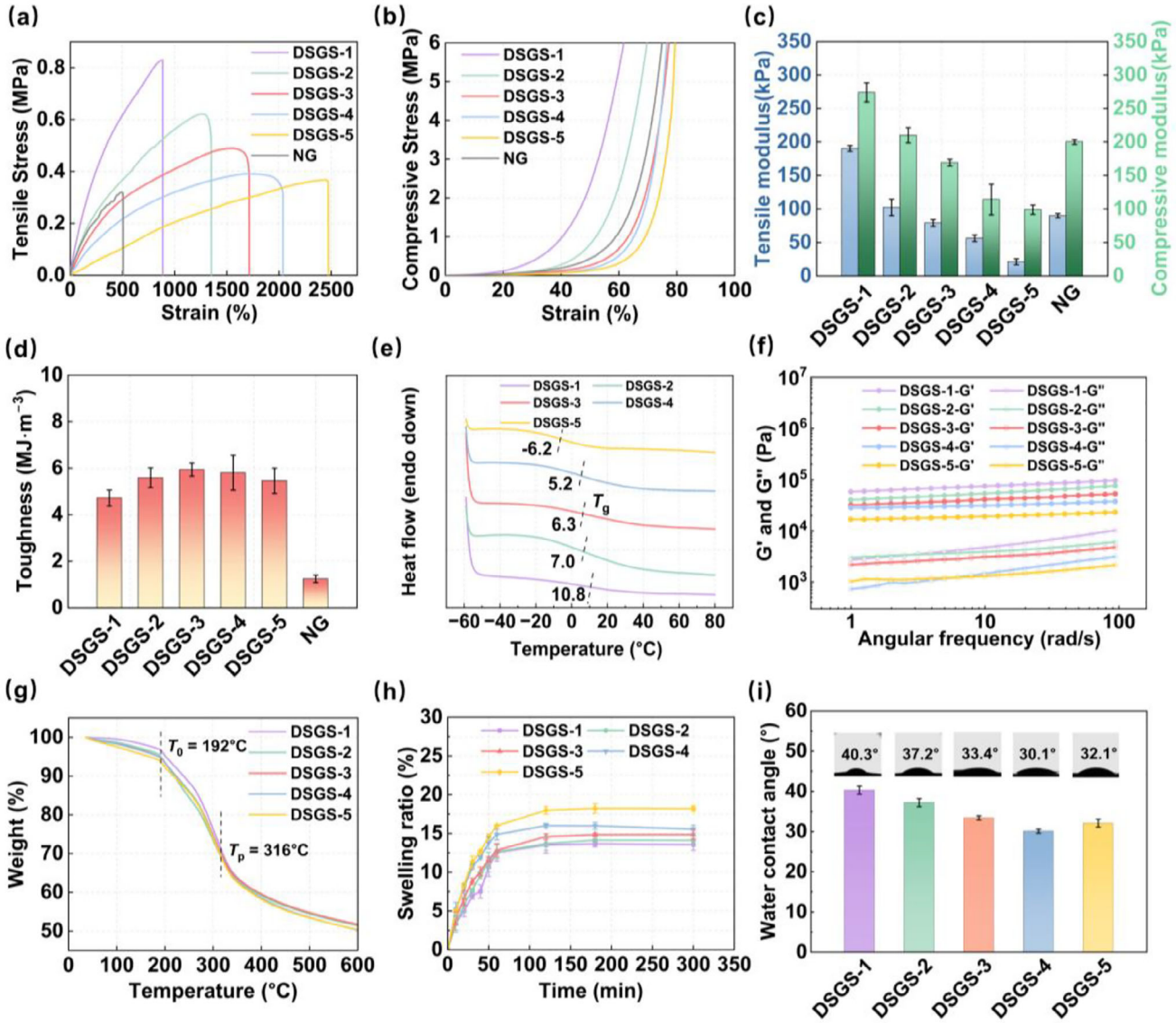

FIGURE 3 | Physicochemical properties of DSGS. (a) Tensile stress–strain curves of DSGSs with different PA contents. (b) Compressive stress–strain curves of DSGSs with different PA contents. (c) Tensile modulus and compressive modulus of DSGSs with different PA contents ($n = 4$). (d) Toughness of DSGSs with different DESs ($n = 4$). (e) DSC spectra of DSGS with different DESs. (f) G′ and G′′ of DSGSs tested under variable shear rates via rheological measurements. (g) Thermal stability of DSGSs. (h) Swelling ratio of DSGSs with different PA contents ($n = 4$). (i) Hydrophilicity of DSGSs with different PA contents evaluated by water contact angle measurements ($n = 3$). Data are presented as means ± SD.

network by binding to the polymer chains via hydrogen atoms. However, the spatial displacement of PA limits its further integration with the PNAGA network, leading to the establishment of hydrogen-bonded shielding networks between the PNAGA chains (Figure 2k).

2.2 | Physicochemical Properties of DSGSs

The influence of the DES's structure on the properties of the DSGSs was investigated. A PNAGA–gelatin (NG) hydrogel was synthesized as a control. As shown in Figure 3a–d, the incorporation of DES significantly enhances the mechanical properties compared to those of the NG hydrogel. Moreover, the mechanical performance of the DSGSs can be modulated by adjusting the DES composition. With increasing PA content in the DES, the tensile strength of the DSGS decreases from 0.83 to 0.37 MPa (Figure 3a); the corresponding compressive strength decreases from 8.60 to 0.57 MPa (Figure 3b); and the tensile and compressive modulus also decrease (Figure 3c). This demonstrates that the multiple hydrogen-bonded shielding network between PA and PNAGA affects the entanglement of the polymer chains, reducing the cross-linking density [29]. Specifically, the abundant hydrogen bond donor groups in PA can strongly interact with the amide groups along the PNAGA chains (Figure 2h,i), forming a dynamic and reversible hydrogen-bonding network. This network creates a "shielding layer" around the polymer chains, thereby weakening direct interchain interactions, such as physical entanglement and interchain cross-linking [29]. Simultaneously, the network enhances the flexibility of the polymer chains, enabling DSGS to achieve a maximum toughness of 5.94 MJ·m^{-3} (Figure 3d). Notably, the tensile modulus of the DSGSs range from 21 to

190 kPa, and the compressive modulus range from 99 to 240 kPa, making them suitable for use in various parts of the eye (10–300 kPa) [30]. Figure 3e illustrates the effect of the PA content on the T_g of the DSGSs. As the PA content in the DES increases, T_g decreases significantly, eventually reaching −6.2°C, confirming the substantial plasticizing effect of PA on the DSGSs. The results also indicate that DES imparts certain anti-freeze properties to the DSGSs [31].

Rheological experiments were performed to further analyze the influence of the DES's structure (Figure 3f). Across the entire frequency range, the G′ values exceed the G″ values, and the G′ values are independent of frequency, reflecting the stability of the hydrogen-bonded shielding networks between PA and PNAGA [32]. These results also indicate that the DSGSs can withstand low-frequency (<100 rad/s) vibrations. Figure S7 shows the XRD patterns of DSGSs with different PA contents. All samples exhibit amorphous structures; as the PA content increases, more distinct amorphous regions are observed, indicating that the hydrogen-bonded shielding networks are amorphous.

The stability of the gels is an important criterion for their application. The thermogravimetry results in Figure 3g show that all DSGSs exhibit good thermal stability, beginning to decompose at 192°C (T_0), with a maximum decomposition rate observed at approximately 316°C (T_p). In addition, the swelling ratios of the DSGSs were determined (Figure 3h). The samples exhibit low swelling ratios (<20%), further confirming the stability of the internal hydrogen bonds. Moreover, the DSGS volume shows no significant change after three days of swelling (Figure S8). The low swelling ratios indicate that the DSGSs can maintain fixed shapes and dimensions. This could reduce the pressure on surrounding tissues in application scenarios, implying that they are suitable for implantation into the body [33]. As shown in Figure 3i, the water contact angles of the DSGSs are between 30° and 40°. This indicates good hydrophilicity, which helps alleviate foreign body reactions and fibrous encapsulation [34]. Ultimately, DSGS-3 was chosen for further functional validation because of its optimal combination of properties, including an ocular tissue-matched modulus, high toughness, good thermal stability, low swelling ratio, and favorable hydrophilicity.

2.3 | MMP-2/Temperature Dual-Responsivity and Adhesion Properties of DSGS

First, the MMP-2 responsiveness of DSGS was tested. During postoperative wound healing, MMP-2 plays a critical role in physiological processes, such as cell migration and tissue remodeling [35]. Moreover, the levels of MMP-2 secreted by cells change dynamically and are regulated by intracellular and extracellular mechanisms at different stages [36]. The MMP-2-responsive degradation of DSGSs occurs; therefore, it is necessary to evaluate the degradation of eutectogels under various MMP-2 concentrations. Different concentrations of MMP-2 were used to measure the in vitro degradation rate of DSGS. For comparison, a eutectogel without gelatin (P-DES) was also synthesized. As shown in Figure 4a, the degradation rate of the DSGS increases significantly after the addition of MMP-2. At an MMP-2 concentration of 1000 ng/mL, the degradation rate exceeds 70% within 7 days while at 100 ng/mL, the degradation rate is 51.9% after 14 days. At a lower MMP-2 concentration (50 ng/mL), the degradation rate of DSGS also reaches 40% at 14 days. In contrast, DSGS without MMP-2 degrades slowly, with a degradation rate of only 15.9% after 7 days and 31.3% after 21 days. The degradation rate of P-DES is not significantly affected by the presence of MMP-2, indicating that gelatin is the key factor enabling MMP-2-responsive degradation. Gelatin is rich in collagen, which is susceptible to hydrolysis in the presence of MMP-2 [37], leading to overall disintegration of the gel.

The influence of MMP-2 on the structure of DSGS was analyzed using swelling experiments. The scanning electron microscopy (SEM) images in Figure 4b show that upon the addition of MMP-2, the originally dense structure of the DSGS becomes porous, with pore sizes of approximately 15 μm. As shown in Figure 4c, the addition of MMP-2 significantly increases the swelling ratio of DSGS, whereas it has almost no effect on P-DES. This indicates that MMP-2 disrupts the internal structure of DSGS by affecting the gelatin framework. The controlled drug release capability of DSGS was evaluated based on the MMP responsivity of the DSGS. Small-angle X-ray scattering (SAXS; Figure S9) profiles show no crystalline diffraction peaks for DSGS-C, indicating excellent dispersion of the drug within the matrix and confirming the great drug-loading efficacy of DSGS. Furthermore, DSGS modulates the drug release rate according to the concentration of MMP-2. As illustrated in Figure 4d, the presence of MMP-2 markedly accelerates drug release from DSGS-C. Compared with the MMP-free group, DSGS-C exposed to 100 ng/mL MMP-2 and 50 ng/mL MMP-2 exhibit significantly higher cumulative release throughout the entire observation period. In summary, the developed DSGS exhibits sensitive MMP responsivity based on a mechanism of gelatin decomposition, which results in the collapse of the overall material structure, thereby enabling controlled drug release.

Subsequently, the temperature responsivity of the DSGS was investigated. Figure 4e shows the trends in the G′ and G″ of DSGS as a function of temperature. As the temperature increases, both G′ and G″ of the DSGS decrease, indicating its temperature sensitivity. Subsequently, the temperature-dependent tensile properties of the DSGS were tested. As shown in Figure 4f, when the temperature increases from 25°C to 50°C, the tensile strength of DSGS decreases, whereas the elongation at break increases, indicating the enhanced flexibility of the gel and a sparser hydrogen-bonded crosslinked network at higher temperatures. This is attributed to the dynamic nature of hydrogen bonds, which dissociate at high temperatures and recombine at lower temperatures [24]. Finally, the effect of temperature on the drug-release behavior of DSGS was investigated. In vitro experiments revealed that the drug release rate from DSGS increases with increasing temperature (Figure 4g). The release of drug molecules from DSGS follows Fick's law of diffusion [38]. As the temperature increases, the cross-linking density of DSGS decreases, leading to a larger pore size within the network. This expansion reduces the frequency of collisions between the drug molecules and polymer chains, thereby increasing the diffusion coefficient of the drug and ultimately increasing the release rate.

Strong adhesion is crucial for drug delivery [39]. The adhesive force enables the system to resist displacement caused by fluid flushing (e.g., by aqueous humor) and physical stresses (e.g.,

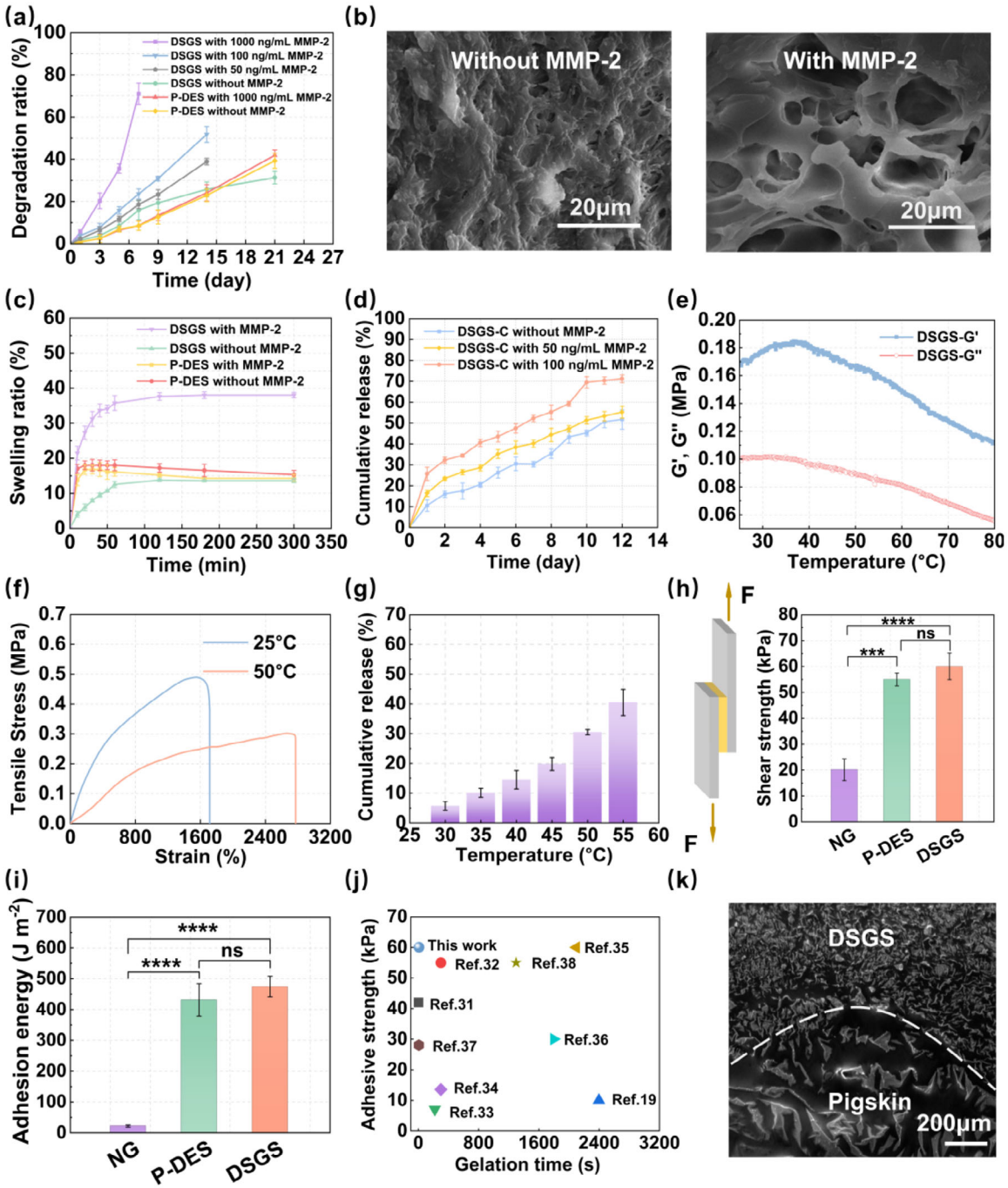

FIGURE 4 | MMP-2/Temperature dual-responsiveness and tissue adhesion of DSGS. (a) Degradation rates of DSGS and P-DES at different MMP-2 concentrations ($n = 4$). (b) SEM images of DSGS before and after incubation with MMP-2 (1000 ng/mL) for 3 days. (c) Swelling ratios of DSGS and P-DES before and after the addition of MMP-2 ($n = 4$). (d) Drug release profiles of DSGS-C as a function of time at 37°C, before and after MMP-2 addition ($n = 3$). (e) G′ and G″ of DSGS as a function of temperature. (f) Tensile stress–strain curves of DSGS at 25°C and 50°C. (g) Cumulative drug release of DSGS-C over 24 h at different temperatures ($n = 3$). (h) Shear strength of NG, P-DES, and DSGS on porcine skin ($n = 4$). (i) Adhesion energy of NG, P-DES, and DSGS on porcine skin ($n = 4$). (j) Gelation time and adhesive strength of DSGS compared with other reported adhesive gels. (k) SEM image of the DSGS-tissue adhesion interface. Data are presented as means ± SD, ns = no significance, ***$p < 0.001$, and ****$p < 0.0001$.

eye blinking), thereby ensuring its stable retention at the target site. In this study, pigskin was used to simulate human skin, and the adhesion between DSGSs with different compositions and pigskin was tested using lap shear tests. Based on the rapid photocuring ability of the DSGS, the precursor was coated onto the tissue surface and cured under UV light to form a eutectogel. As shown in Figure 4h and Figure S10, the DSGS exhibits robust adhesion, with an adhesion strength of up to 60.1 kPa on dry skin. P-DES also exhibits good tissue adhesion. In contrast, the NG hydrogel without DES exhibits a much lower adhesive strength of only 20.2 kPa on dry skin, demonstrating that the incorporation of DES, and particularly the formation of hydrogen-bonded shielding networks, significantly enhances the adhesion performance of the gel. DSGS maintains substantial

adhesion to wet skin, with an adhesion strength of 45.2 kPa (Figure S11). The adhesion between the conjunctiva and DSGS determines the long-term therapeutic performance of DSGS in the eye. As shown in Figures S12 and S13, the adhesion strength of DSGS to the conjunctiva is 32.5 kPa, providing a basis for subsequent in vivo experiments.

The peeling adhesion energy between biological tissue and DSGS, P-DES, or NG was measured. DSGS exhibits a peeling adhesion energy of 474.45 $J \cdot m^{-2}$, which is significantly higher than that of the NG hydrogel (Figure 4i, Figure S14). To further verify the adhesive performance of DSGS to diverse substrates, we attached a 1 mm-thick DSGS film to a volunteer's finger and brought it into contact with the heart, liver, spleen, lungs, and kidneys of mice; ethical approval was obtained for all experiments involving humans and animals. The results show that DSGS firmly adheres to the surfaces of various organs (Figure S15). Compared with most reported adhesive gels [26, 40–47], DSGS exhibits a faster gelation time and higher adhesive strength (Figure 4j).

The abundant amide and phosphate groups on the DSGS surface form hydrogen bonds with amino and carboxyl groups in biological tissues, which play an important role in adhesion (Figure S16). Microstructural analysis of the DSGS–tissue interface reveals tight integration between the DSGS and tissue, with no visible gaps or voids, indicating a mechanically interlocked structure (Figure 4k, Figure S17) [32]. This effective integration is attributed to the in situ gelation method, which promotes multiple interactions between the DSGS and tissue. Furthermore, the DSGS exhibits satisfactory tensile strength (0.49 MPa, Figure 2a), indicating that its strong adhesion stems from the combined effect of robust interfacial bonding and high cohesive energy [32].

2.4 | Biological Function Validation, Immunomodulatory Effects, and 4D Printing Capabilities of DSGS

First, the biocompatibility of DSGS was evaluated. Live/dead staining was performed to assess the biocompatibility of DSGS by examining the viability of rabbit primary conjunctival fibroblasts co-cultured with the material. Live/dead staining images (Figure 5a) show abundant viable cells (green) and a few dead cells (red) in all groups, with no observable differences, whereas Cell Counting Kit-8 (CCK-8) assays (Figure 5b) confirm high cell viability (>90%) across days 1–3. These results indicate that DSGS provides a favorable microenvironment for cell growth with low cytotoxicity [48]. To enhance the clinical relevance of this study, the biocompatibility of DSGS was further evaluated using human scleral fibroblasts (HSFs). The results demonstrate that DSGS exhibits excellent cytocompatibility in HSFs, with no significant impact on cell viability and no observable cytotoxicity (Figure S18). These findings are consistent with those obtained from rabbit primary conjunctival fibroblasts, further supporting the safety and potential clinical applicability of DSGS in human ocular tissues.

Immunofluorescence analysis of macrophage polarization after three days of culture (Figure 5c) shows that the control group exhibits strong inducible nitric oxide synthase (iNOS; M1) and weak Arginase-1 (Arg-1; M2) signals, whereas the CCR2 inhibitor (CCR2i), DSGS, and DSGS-C treatments reduced iNOS and enhanced Arg-1 fluorescence, with DSGS-C showing the most pronounced effect. This suggests that DSGS-C effectively suppresses M1 activation and promotes M2 polarization, whereas DSGS alone confers notable anti-inflammatory effects.

The analysis of α-smooth muscle actin (α-SMA) expression (Figure 5d,e) reveals robust myofibroblast activation in the control samples, which is significantly inhibited by both DSGS and DSGS-C, with DSGS-C exerting the strongest suppression. These findings indicate that DSGS-based eutectogels maintain fibroblast viability and modulate fibroblast-to-myofibroblast transition, a key process in scar formation [49].

The excessive suppression of normal fibroblast viability impairs physiological wound healing, leading to tissue instability. DSGS and DSGS-C exhibit excellent biocompatibility and low cytotoxicity, while exerting notable immunomodulatory effects. Both materials promote macrophage polarization toward an M2-dominant phenotype, which can reduce proinflammatory cytokine release and support balanced wound healing. DSGS-C shows the strongest effect on macrophage reprogramming, likely due to the controlled release of a CCR2 inhibitor that disrupts the CCL2–CCR2 axis, thereby inhibiting monocyte/macrophage recruitment and M1 polarization [50]. Moreover, both DSGS and DSGS-C effectively suppress fibroblast-to-myofibroblast transition, as indicated by reduced α-SMA expression, a key step in scar formation [51]. Collectively, eutectogels, particularly DSGS-C, combine intraocular biocompatibility with immunoregulatory activity, stabilize the inflammatory microenvironment, and mitigate fibrotic responses.

These properties suggest that the developed DSGS may prolong bleb function and reduce surgical failure after GDD implantation, warranting further long-term in vivo studies to evaluate their clinical translation. The rapid photocuring capability of DSGS enables it to be 4D-printed to fabricate a novel medical device with customizable shapes and responsive drug release. Based on this, we used 4D printing technology to prepare DSGS and DSGS-C into GDDs (Figure 5f,g), which were named 4D DSGS and 4D DSGS-C, respectively, for subsequent in vivo validation.

2.5 | The Application of 4D Printing GDD in Preventing Postoperative Scarring After Glaucoma Surgery

To evaluate the anti-scarring efficacy of the CCR2i, 4D DSGS, and 4D DSGS-C after glaucoma surgery, histological, immunofluorescence, and functional analyses were performed at the early (5 days) and late (28 days) postoperative stages and compared with Ahmed glaucoma valve (AGV; a commonly used GDD in glaucoma surgery). As shown in Figure 6a, hematoxylin and eosin (H&E) and Masson's trichrome staining images reveal marked bleb wall thickening and excessive collagen deposition in the AGV group, whereas CCR2i, 4D DSGS, and 4D DSGS-C treatment significantly attenuate fibrotic remodeling at both time points. Among these interventions, 4D DSGS-C consistently exhibits the greatest reduction in bleb wall thickness and collagen accumulation, indicating a synergistic antifibrotic effect [52].

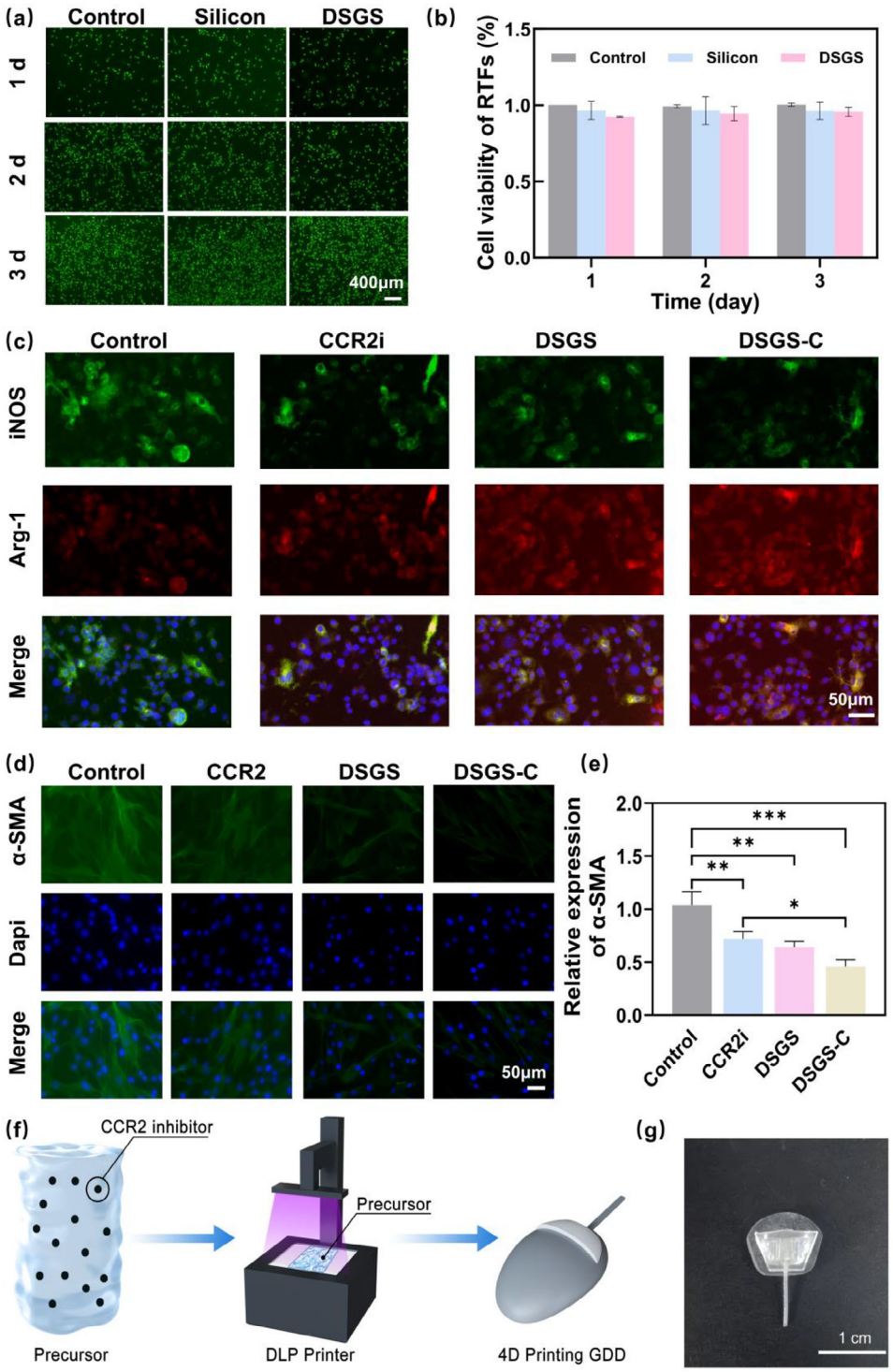

FIGURE 5 | Biological function validation, immunomodulatory effects, and 4D printing capabilities of DSGS. (a) Live/dead staining of RTFs cultured with control medium, silicone, and DSGS hydrogel for 1, 2, and 3 days. (b) Cell viability assessed by CCK-8 assay over 3 days ($n = 3$). (c) Immunofluorescence staining of macrophage polarization markers: iNOS (green), Arg-1 (red), and nuclei (DAPI, blue) after different treatments. (d) Immunofluorescence staining of α-SMA (green) in fibroblasts with DAPI nuclear counterstaining. (e) Quantification of α-SMA fluorescence intensity ($n = 3$). (f) Schematic diagram of the preparation of a 4D printing GDD. (g) Photograph of the novel GDD. Data are presented as means ± SD, $^{*}p < 0.05$, $^{**}p < 0.01$, and $^{***}p < 0.001$.

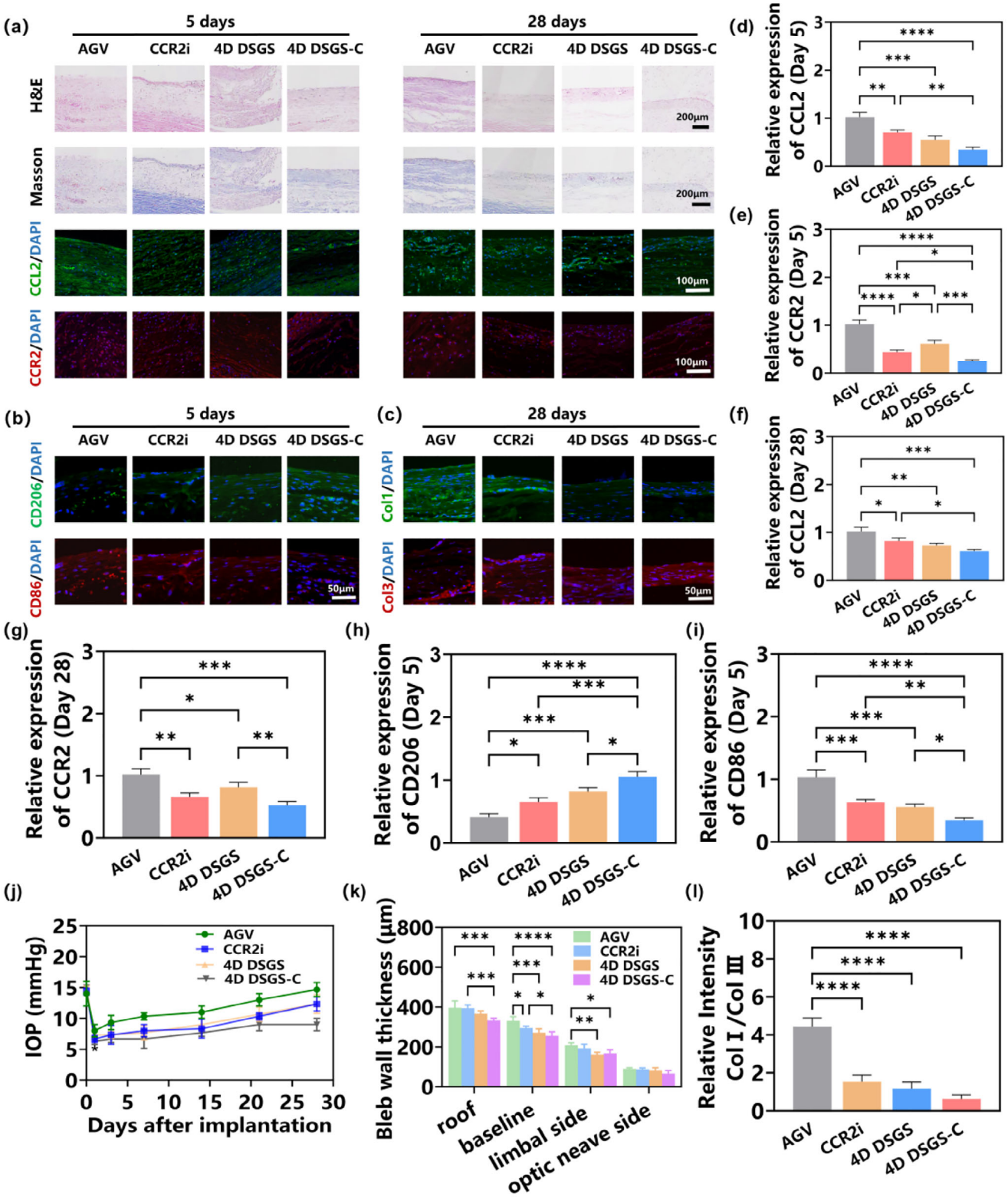

FIGURE 6 | 4D printing GDDs attenuate postoperative inflammation and fibrosis in vivo. (a) Representative H&E and Masson's trichrome staining of filtering blebs at 5 and 28 days after implantation in different treatment groups. Immunofluorescence staining of CCL2 (green), CCR2 (red), and nuclei (DAPI, blue) is shown in the lower panels. (b) Immunofluorescence staining of macrophage markers CD206 (green) and CD86 (red) with DAPI counterstaining at 5 days post-implantation. (c) Immunofluorescence staining of collagen I (Col I, green) and collagen III (Col III, red) at 28 days after surgery. (d-i) Relative expression of CCL2, CCR2, CD206 and CD86. (j) IOP changes over time in different groups. (k) Quantification of bleb wall thickness at different anatomical regions at 28 days post-operation. (l) Relative intensity of Col-I /Col-III (d-l, $n = 6$). Data are presented as means ± SD, $^{*}p < 0.05$, $^{**}p < 0.01$, $^{***}p < 0.001$ and $^{****}p < 0.0001$.

Postoperative inflammation was further assessed using immunofluorescence staining of the CCL2–CCR2 axis. As shown in Figure 6ad–g, strong CCL2 and CCR2 expression is observed in the AGV group, reflecting the persistent activation of inflammatory signaling after surgery. In contrast, CCR2i, 4D DSGS, and 4D DSGS-C markedly suppress the expression of CCL2 and CCR2, with 4D DSGS-C exhibiting the most pronounced inhibitory effect. These findings suggest that the sustained modulation of the CCL2–CCR2 pathway effectively limits inflammatory cell recruitment at the bleb site, thereby reducing downstream fibrotic responses [53].

Macrophage polarization was further examined at 5 days postoperatively (Figure 6b,h,i). Compared with the AGV group, 4D DSGS and 4D DSGS-C treatment significantly reduced the expression of the M1-associated marker CD86 while enhancing the expression of the M2 marker CD206, indicating a shift toward an anti-inflammatory macrophage phenotype [54]. Notably, 4D DSGS-C induced the most prominent macrophage polarization, highlighting the critical role of CCR2 inhibition in regulating early postoperative inflammation.

Importantly, these structural and immunological improvements translate into functional benefits. As shown in Figure 6j, the AGV group exhibits a higher postoperative IOP than the other treatment groups. CCR2i, 4D DSGS, and 4D DSGS-C effectively reduce bleb wall thickening and preserve subconjunctival outflow, with 4D DSGS-C achieving the lowest and most stable IOP, indicating its superior functional efficacy.

The quantitative analysis further confirms these findings. As shown in Figure 6k, the bleb wall thickness was significantly reduced in all treatment groups compared with that in the AGV group. Collagen subtype analysis (Figure 6c,l) reveals a markedly elevated collagen I/III ratio in the AGV group, indicating excessive fibrotic scar formation and impaired wound healing [55]. In contrast, the CCR2i, 4D DSGS, and 4D DSGS-C groups exhibit collagen I/III ratios close to 1, comparable to those of normal tissue remodeling, suggesting improved healing quality and reduced pathological scarring [56].

Collectively, these results demonstrated that 4D DSGS-C effectively mitigates postoperative scarring by suppressing CCL2–CCR2 mediated inflammation, promoting macrophage polarization toward a reparative phenotype, normalizing collagen remodeling, and preserving filtering bleb structure and function. The integration of a biocompatible eutectogel matrix with targeted CCR2 inhibition provides a synergistic strategy for regulating inflammation and fibrosis, ultimately improving the long-term surgical outcomes.

2.6 | Injectability and Biological Validation of DSGS

The rapid change in the G′ of the precursor upon light irradiation (Figure 1f) confers injectability. When the precursor is irradiated for less than 10 s, it exhibits liquid-like behavior. The precursor exhibits low viscosity (0.01 Pa s) without irradiation, which is unfavorable for shape retention (Figure S19). After 10 s of irradiation, the viscosity of the DSGS reaches approximately 35 Pa·s, achieving a balance between flowability and shape preservation. Thus, an injectable DSGS can be obtained. Figure 7a schematically illustrates the preparation process for injectable DSGS. As shown in Figure S20, a sharp decrease in the viscosity of the injectable DSGS is observed with increasing shear rate at low shear rates, and the low viscosity is maintained at high shear rates, demonstrating its favorable fluidity within a syringe [28]. In the alternating step strain scan test (Figure S21), the injectable DSGS transitions to a liquid state ($G' < G''$) at an increased strain (1000%), and when the strain is reduced to 10%, the values of G′ and G″ recover to their original state, indicating that the mechanical properties of DSGS undergo a complete and instantaneous recovery, which is consistent with the characteristics of injectable gels [57]. Furthermore, the shape-forming capability of the injectable DSGS was investigated. As depicted in Figure S22, the injectable DSGS was extruded through a syringe onto a plate to clearly write "HIT." Additionally, we injected DSGS into porcine muscle tissue in different shapes (circle and square) and performed bending and twisting of the overlying skin (Figure 7b). The DSGS remained firmly adhered, exhibiting excellent flexibility and the ability to deform with the tissue. The injectable DSGS can fill irregular defects (Figure 7c), highlighting its exceptional self-adaptability. Notably, the injected DSGS allows the modulation of its mechanical properties through secondary in situ photocuring, thereby adapting to the target site (Figure S23).

The in vivo retention of the injectable gels was evaluated by monitoring ocular localization over time after injection. As shown in Figure 7d, both the injectable DSGS and DSGS-T remain clearly localized at the injection site up to 30 days post-injection, whereas the saline and timolol solutions were rapidly absorbed and were no longer detectable within minutes. This observation demonstrates that the eutectogel matrix can effectively anchor within the ocular tissues, providing a stable platform for sustained drug exposure. The prolonged retention of DSGS-T indicates its potential to maintain consistent contact with target tissues [58], which is critical for achieving long-term therapeutic effects in glaucoma management.

The compatibility of the injectable DSGS with ocular tissue was evaluated by histological analyses of the cornea, ciliary body, and conjunctiva (Figure 7e). No evidence of inflammatory cell infiltration, edema, or structural abnormalities was observed in any treatment group, confirming that both the eutectogel and eutectogel–drug formulations were biocompatible and safe for intraocular use [59]. These findings support the suitability of DSGS-based systems for long-term ocular implantation, without inducing local tissue toxicity.

The drug-release behavior of the eutectogel was further characterized by examining the cumulative release of timolol from DSGS-T over one month (Figure 7f). The release profile exhibits a gradual and sustained pattern, with approximately 82% of the loaded timolol released by day 30. This controlled release suggests that DSGS-T maintains therapeutic drug concentrations in the ocular microenvironment over extended periods, potentially reducing the frequency of topical administration and improving patient compliance. The release kinetics likely result from the dense polymer network of DSGS, which provides a diffusion barrier and regulates drug mobility [60].

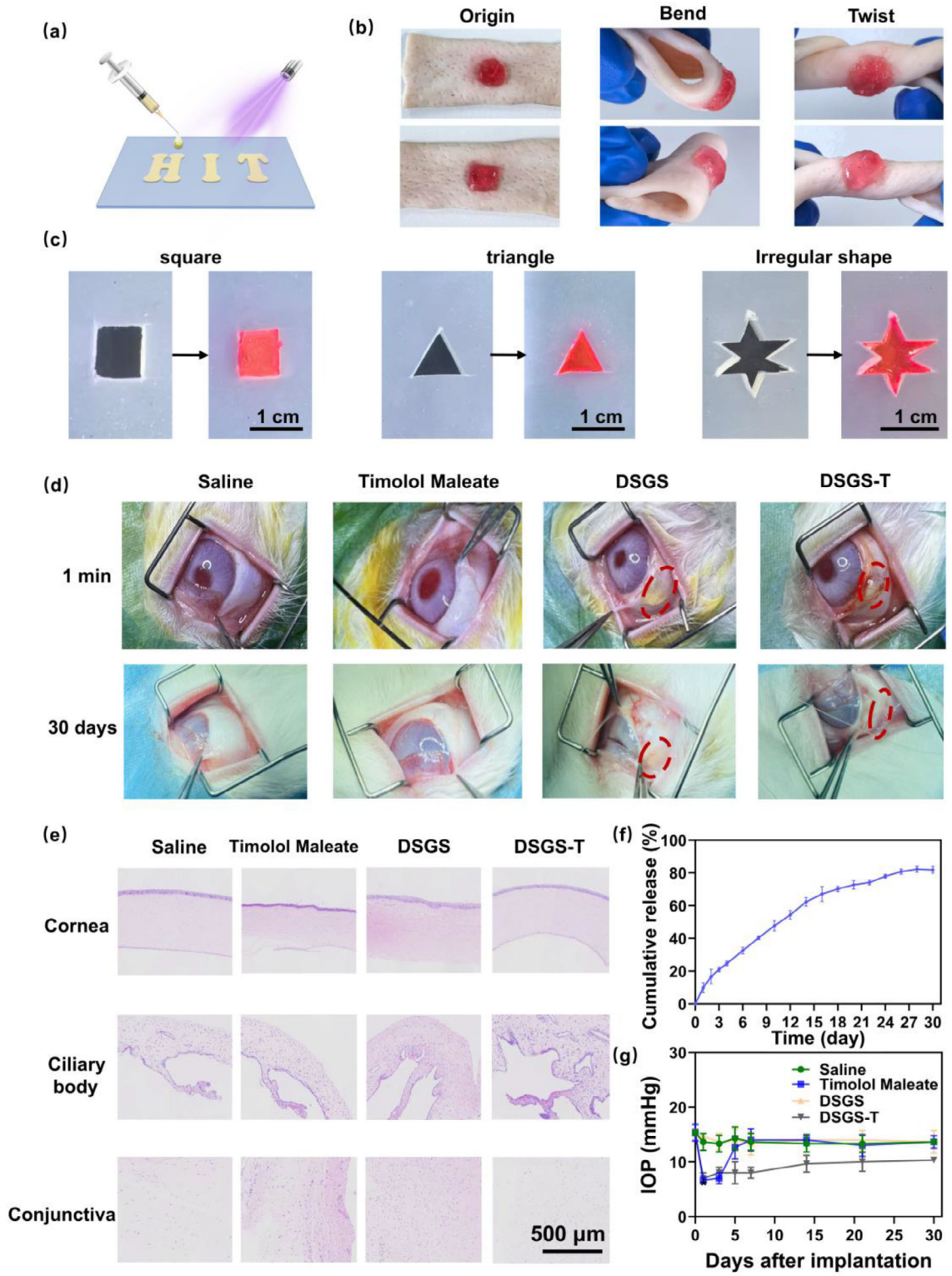

FIGURE 7 | Injectable DSGS: Adaptability and in vivo glaucoma treatment. (a) Schematic diagram of injectable DSGS preparation. (b) Photographs of DSGS injected into porcine skin in different shapes, showcasing its overall state under bending and twisting deformations. (c) Photographs of injectable DSGS filling regular-shaped wounds. (d) Images of different materials after injection into the rabbit conjunctiva and after 30 days. (e) In vivo safety analysis. (f) In vitro drug release profile of DSGS-T over time ($n = 3$). (g) Effects of saline, timolol maleate solution, DSGS, and DSGS-T on IOP ($n = 6$). Data are presented as means ± SD.

The pharmacological efficacy of the eutectogel system was assessed by monitoring the IOP over time (Figure 7g). Both timolol maleate and DSGS-T treatments significantly decrease IOP compared with the saline control, whereas injectable DSGS alone exhibits no effect, confirming that the eutectogel matrix itself does not lower the IOP. Notably, compared to timolol maleate alone, DSGS-T demonstrates a more pronounced reduction in IOP, which is maintained for at least 30 days. This indicates that the eutectogel formulation both prolongs the residence time of the drug and enhances the pharmacodynamic performance of timolol, which is attributed to the combination of sustained release and local retention [61]. These results highlight the advantages of eutectogel-based ocular drug delivery.

Collectively, these data indicate that DSGS-T effectively integrates the injectability and biocompatibility of the eutectogel matrix with sustained timolol delivery, resulting in significant and durable IOP reduction while preserving ocular tissue integrity. The eutectogel functioned as a localized drug reservoir, prolonging therapeutic exposure and enhancing drug efficacy. As shown in Figure S24, stimulation with warm saline at 42°C enables DSGS-T to achieve a more pronounced IOP-lowering effect. This highlights the advantage of the temperature responsiveness of DSGS. Furthermore, the therapeutic efficacy of DSGS loaded with the hydrophobic drug latanoprost (DSGS-L) for glaucoma treatment was evaluated. As shown in Figure S25, DSGS-L rapidly reduces IOP and maintains it at a relatively stable level over a certain period. These results indicate that DSGS can effectively encapsulate hydrophobic drugs and enable their sustained delivery. In addition, the drug loading concentration in DSGS-L is 1 mg/g, which is significantly higher than that of commercially available latanoprost eye drops (0.05 mg/g), demonstrating the advantage of DES in enhancing drug solubility and utilization.

Finally, DSGS with recently reported drug delivery systems for glaucoma treatment was compared. From Table S2, it can be seen that DSGS has a modulus matching that of the human eye, high toughness, and strong adhesion, while enabling intelligent drug release through dual response to MMP-2 and temperature, maintaining low IOP for 30 days. Moreover, DSGS has two molding methods, which can meet the needs of glaucoma patients with different symptoms. These characteristics suggest that DSGS has considerable potential as a long-term treatment strategy for glaucoma, offering advantages over conventional hydrogel-based drug delivery systems in terms of efficacy and patient adherence.

3 | Conclusion

In summary, we present a smart drug delivery system based on the eutectogel to overcome key challenges of traditional drug delivery systems in glaucoma treatment, such as achieving long-term, stable, and controllable drug release. By forming multi-hydrogen-bonded shielding networks between DES and polymer chains, we constructed a DSGS with programmable mechanical strength, high toughness, and strong tissue adhesion. The elastic modulus of DSGS matches ocular tissue properties, offering a stable foundation for long-term implantation. The DSGS exhibits dual responsiveness to both MMP-2 and temperature, enabling precise, pathology-triggered drug release that enhances therapeutic accuracy. Using 4D printing technology, we fabricated the DSGS-C into a GDD that integrates both structure and function. This highlights the potential of smart materials combined with advanced manufacturing in the field of personalized medical devices. Importantly, the resulting GDD modulated the post-operative immune microenvironment and suppressed fibrosis through synergistic material–drug interactions. Additionally, the DSGS-T was injected under the conjunctiva to achieve stable IOP for one month. This work not only provides innovative solutions for glaucoma treatment but also offers valuable insights for research in a wide range of fields such as tissue engineering and targeted drug delivery. Although promising therapeutic outcomes have been observed, this study was conducted in rabbits with normal IOP. Future studies are required to evaluate the anti-fibrotic efficacy and IOP–lowering performance of this smart material in models of sustained ocular hypertension.

4 | Experimental Section

4.1 | Materials

β-Cyclodextrin (98%), phytic acid (90% aqueous solution), gelatin (biotechnology grade), glycinamide hydrochloride (97%), acryloyl chloride (98%), NaOH (99%), and Rhodamine B (AR) were all purchased from Macklin Technology Co., Ltd. (Shanghai, China). Hydrochloric acid (AR), Diethyl ether (AR), methanol (99.5%), and ethanol (99.5%) were all purchased from Fuyu Fine Chemical Co., Ltd. (Tianjin, China). The photoinitiator lithium phenyl-2,4,6-trimethylbenzoylphosphinate (LAP) was purchased from Aladdin Biochemical Technology Co., Ltd. (Shanghai, China). Porcine skin was obtained from a local market. Abaucin hydrochloride (CCR2 inhibitor, 99.9%), (S)-Timolol maleate (99.8%), and Latanoprost (99.8%) were purchased from MedChemExpress (USA). Recombinant matrix metalloproteinase 2 was purchased from Yuanye Technology Co., Ltd. (Shanghai, China). Cyanoacrylate (CA) glue was purchased from Jiangsu Deyuan Technology Co., Ltd. (Yancheng, China). The Cell Counting Kit-8 assay kit was purchased from Meilun Biotechnology Co., Ltd. (Dalian, China). Live/Dead cell viability staining kits were obtained from Beyotime Biotechnology (Shanghai, China). Hematoxylin and eosin staining reagents were purchased from Solarbio Science & Technology Co., Ltd. (Beijing, China), and Masson's trichrome staining kits were obtained from Nanjing Jiancheng Bioengineering Institute (Nanjing, China). Primary antibodies used for immunofluorescence staining were purchased from Proteintech Group, Inc. (Wuhan, China), including anti-iNOS (RRID: AB_2879038), anti-Arg-1 (RRID: AB_1119069), anti-α-SMA (RRID: AB_2223009), anti-CCL2 (RRID: AB_2918100), anti-CCR2 (RRID: AB_2262945), anti-CD206 (RRID: AB_10597232), anti-CD86 (RRID: AB_3670897), anti-Col1 (RRID: AB_2882554) and anti-Col3 (RRID: AB_2935393). New Zealand white rabbits (12 weeks of age, weighing 2–3 kg) were supplied by the Laboratory Animal Research Center of the Second Affiliated Hospital of Harbin Medical University.

4.2 | Preparation of DES

Using DES-1 as an example, 11.11 g of PA (90% aqueous solution) and 5 g of CD were weighed separately and added to a beaker.

The mixture was then stirred at 60°C for 30 min at 300 rpm. The resulting clear and transparent liquid was the DES.

4.3 | Preparation of DSGS

Taking DSGS-1 as an example, 3 g of DES-1 was weighed, and 7 g of deionized water was added to it, followed by mixing until homogeneous. Gelatin, NAGA, and LAP were then added to the solution at weight percentages of 4, 16, and 0.5 wt.%, respectively. The mixture was stirred in a magnetic stirring water bath at 50°C for 30 min at a speed of 300 rpm. Then, the DSGS precursor was obtained. Finally, the precursor was poured into a custom-made polytetrafluoroethylene mold and exposed to a UV lamp (405 nm, 10 mW cm^{-2}) for 2 min to obtain DSGS-1.

The DSGS precursor was exposed to a UV lamp (405 nm, 10 mW cm^{-2}) for 10 s to obtain injectable DSGS.

4.4 | Preparation of DSGS-C

A CCR2 inhibitor powder was added to the precursor solution of DSGS-3 and mixed uniformly to achieve a drug concentration of 1 μg/mL. The same light irradiation procedure used for the preparation of DSGS was then applied to obtain DSGS-C.

4.5 | Preparation of DSGS-T

Timolol maleate powder was added to the DSGS-3 precursor at a drug concentration of 1 mg/mL and mixed thoroughly. Then, the mixture was poured into a custom-made polytetrafluoroethylene mold and exposed to a UV lamp (405 nm, 10 mW cm^{-2}) for 10 s to obtain DSGS-T.

4.6 | Preparation of DSGS-L

Ten milligrams of latanoprost was uniformly mixed with 3 g of DES-3, followed by the addition of 7 g of deionized water. Complete dissolution of the drug was confirmed by UV–vis spectrophotometry (UV5Nano, METTLER TOLEDO, Switzerland), resulting in a drug concentration of 1 mg/g. Gelatin, NAGA, and LAP were then added to the solution at weight percentages of 4 wt%, 16 wt%, and 0.5 wt%, respectively. The mixture was stirred in a magnetic stirring water bath at 40°C for 60 min at a speed of 300 rpm. Then, the mixture was poured into a custom-made polytetrafluoroethylene mold and exposed to a UV lamp (405 nm, 10 mW cm^{-2}) for 10 s to obtain DSGS-L.

4.7 | Characterization

The viscosity of the DESs was tested using a viscometer (DVNX-HBCBG, Brookfield, USA). ^{1}H NMR spectra were recorded on a spectrometer (Bruker Avance III, Germany). XRD patterns from 0° to 90° were measured using a diffractometer (Rigaku-2038, Japan). Thermal properties were evaluated by a thermogravimetric analysis-differential scanning calorimetry (TGA/DSC3+, METTLER TOLEDO, Switzerland). Dynamic mechanical analysis (DMA, Q800, TA, USA) was employed to characterize the thermoresponsive behavior of the DSGS. XPS spectra were acquired on a spectrometer (Thermo Scientific K-Alpha, USA). FT-IR spectra were recorded using a spectrometer (Nicolet iS10, Thermo Fisher Scientific, USA). Viscosity changes and rheological behavior were examined with a rotational rheometer (DHR2, TRIOS, Germany). The adhesive interface between DSGS and tissue was observed by an optical microscope (Bositonli, China). The microstructure of the DSGSs was examined with a scanning electron microscope (SEM, Hitachi SU5000, Japan). Small-angle X-ray scattering (SAXS, Xenocs Xeuss 3.0, France) was employed to evaluate the dispersion state of the drug within the DSGS. The optical contact angle measurement system (Theta, Finland) was used to test the hydrophilicity of DSGS.

4.8 | Ethics Approval

Animal procedures were reviewed and authorized by the Animal Ethics Committee of the Second Affiliated Hospital of Harbin Medical University (Approval No. YJSDW2023-202). All experiments complied with the ARVO Statement for the Use of Animals in Ophthalmic and Vision Research and followed the ARRIVE guidelines.

4.9 | Additional Methods

Experimental details regarding the mechanical property tests, adhesion performance tests, biological function validation of DSGS, and so on are provided in the Supporting Information.

Acknowledgements

The authors acknowledge the support by the Heilongjiang Provincial Natural Science Foundation of China (Grant No. 2022ZX02C25).

Conflicts of Interest

The authors declare no conflicts of interest.

Data Availability Statement

The data that support the findings of this study are available from the corresponding author upon reasonable request.

References

1. R. N. Weinreb, C. K. S. Leung, J. G. Crowston, et al., "Primary Open-Angle Glaucoma," *Nature Reviews Disease Primers* 2 (2016): 16067, https://doi.org/10.1038/nrdp.2016.67.

2. H. E. Killer and A. Pircher, "Normal Tension Glaucoma: Review of Current Understanding and Mechanisms of the Pathogenesis," *Eye* 32 (2018): 924–930, https://doi.org/10.1038/s41433-018-0042-2.

3. K. Mansouri, F. A. Medeiros, and R. N. Weinreb, "Global Rates of Glaucoma Surgery," *Graefe's Archive for Clinical and Experimental Ophthalmology* 251 (2013): 2609–2615, https://doi.org/10.1007/s00417-013-2464-7.

4. J. O. Abaricia, N. Farzad, T. J. Heath, J. Simmons, L. Morandini, and R. Olivares-Navarrete, "Control of Innate Immune Response by Biomaterial

Surface Topography, Energy, and Stiffness," *Acta Biomaterialia* 133 (2021): 58–73, https://doi.org/10.1016/j.actbio.2021.04.021.

5. Y. Han, Q. Geng, A. Dong, et al., "Anti-Scar Effects of Micropatterned Hydrogel After Glaucoma Drainage Device Implantation," *Research* 8 (2025): 0561, https://doi.org/10.34133/research.0561.

6. H. Kondo, H. Tazawa, T. Fujiwara, et al., "Osteosarcoma Cell–Derived CCL2 Facilitates Lung Metastasis via Accumulation of Tumor-Associated Macrophages," *Cancer Immunology, Immunotherapy* 74 (2025): 193, https://doi.org/10.1007/s00262-025-04051-x.

7. M. Dang, K. V. Slaughter, H. Cui, et al., "Colloid-Forming Prodrug-Hydrogel Composite Prolongs Lower Intraocular Pressure in Rodent Eyes After Subconjunctival Injection," *Advanced Materials* 37 (2025): 2419306, https://doi.org/10.1002/adma.202419306.

8. X. Luan, X. Zhang, Q. Luan, J. Gan, Y. Wang, and Y. Zhao, "Traditional Chinese Medicine Integrated Multifunctional Responsive Core–Shell Microneedles for Dermatosis Treatment," *Research* 7 (2024): 0420, https://doi.org/10.34133/research.0420.

9. Y. Wu, J. Mao, Y. Zhou, et al., "Youthful Brain-Derived Extracellular Vesicle-Loaded GelMA Hydrogel Promotes Scarless Wound Healing in Aged Skin by Modulating Senescence and Mitochondrial Function," *Research* 8 (2025): 0644, https://doi.org/10.34133/research.0644.

10. W. Wu, J. Zhang, X. Qu, et al., "Enabling Targeted Drug Delivery for Treatment of Ulcerative Colitis With Mucosal-Adhesive Photoreactive Hydrogel," *Advanced Science* 12 (2025): 2404836, https://doi.org/10.1002/advs.202404836.

11. S. Chen, W. Yao, Z. Ding, et al., "Injectable Electrospun Fiber-Hydrogel Composite Delivery System for Prolonged and Nociceptive-Selective Analgesia," *Advanced Fiber Materials* 6 (2024): 1428–1445, https://doi.org/10.1007/s42765-024-00422-8.

12. R. Song, X. Wang, M. Johnson, et al., "Enhanced Strength for Double Network Hydrogel Adhesive Through Cohesion-Adhesion Balance," *Advanced Functional Materials* 34 (2024): 2313322, https://doi.org/10.1002/adfm.202313322.

13. Y. Hu, W. Yang, J. Zhan, C. Pu, L. Zhong, and H. Hou, "Eutectogels: Recent Advances and Emerging Biological Applications," *Advanced Functional Materials* 35 (2025): 2425778, https://doi.org/10.1002/adfm.202425778.

14. M. L. Picchio, M. S. Orellano, M. A. Motta, et al., "Elastomeric Protein Bioactive Eutectogels for Topical Drug Delivery," *Advanced Functional Materials* 34 (2024): 2313747, https://doi.org/10.1002/adfm.202313747.

15. D. O. Abranches, L. P. Silva, M. A. R. Martins, S. P. Pinho, and J. A. P. Coutinho, "Understanding the Formation of Deep Eutectic Solvents: Betaine as a Universal Hydrogen Bond Acceptor," *Chemsuschem* 13 (2020): 4916–4921, https://doi.org/10.1002/cssc.202001331.

16. P. A. Mercadal, A. González, A. Beloqui, et al., "Eutectogels: The Multifaceted Soft Ionic Materials of Tomorrow," *JACS Au* 4 (2024): 3744–3758.

17. G. Balenzano, G. F. Racaniello, I. Arduino, et al., "Cyclodextrin-Based Supramolecular Deep Eutectic Solvent (CycloDES): A Vehicle for the Delivery of Poorly Soluble Drugs," *International Journal of Pharmaceutics* 647 (2023): 123553, https://doi.org/10.1016/j.ijpharm.2023.123553.

18. S. Xing, G. Zhang, A. Zhang, et al., "Poly(N -acryloyl glycinamide) Eutectogels," *Journal of Polymer Science* 62 (2024): 925–936, https://doi.org/10.1002/pol.20230603.

19. K. Chen, J. Wang, J. Cao, et al., "Enzyme-Responsive Microgel With Controlled Drug Release, Lubrication and Adhesion Capability for Osteoarthritis Attenuation," *Acta Biomaterialia* 190 (2024): 191–204, https://doi.org/10.1016/j.actbio.2024.10.026.

20. C. Hu, J. Ma, X. Chen, et al., "Microenvironment-Driven Transformable Self-Assembly Nanoplatform Enables Spatiotemporal Remodeling for Rheumatoid Arthritis Therapy," *Science Advances* 11 (2025): adu5245, https://doi.org/10.1126/sciadv.adu5245.

21. R. Langer and D. A. Tirrell, "Designing Materials for Biology and Medicine," *Nature* 428 (2004): 487–492, https://doi.org/10.1038/nature02388.

22. L. Ma, Y. Zhu, L. Wang, et al., "Multi-Form Antibacterial Dressings Based on a Deep Eutectic Supramolecular Polymer Promote Healing of Burn Wounds Through a Weakly Acidic Microenvironment," *Chemical Engineering Journal* 494 (2024): 153153, https://doi.org/10.1016/j.cej.2024.153153.

23. H. Wang, S. Liu, Y. Zhao, J. Wang, and Z. Yu, "Insights Into the Hydrogen Bond Interactions in Deep Eutectic Solvents Composed of Choline Chloride and Polyols," *ACS Sustainable Chemistry & Engineering* 7 (2019): 7760–7767, https://doi.org/10.1021/acssuschemeng.8b06676.

24. P. Yao, Q. Bao, Y. Yao, et al., "Environmentally Stable, Robust, Adhesive, and Conductive Supramolecular Deep Eutectic Gels as Ultrasensitive Flexible Temperature Sensor," *Advanced Materials* 35 (2023): 2300114, https://doi.org/10.1002/adma.202300114.

25. D. Duymaz, İ. C. Karaoğlu, and S. Kizilel, "Effect of Photoinitiation Process on Photo-Crosslinking of Gelatin Methacryloyl Hydrogel Networks," *Macromolecular Rapid Communications* 46 (2025): 00376, https://doi.org/10.1002/marc.202500376.

26. K. Zhao, X. Zhao, X. Guo, et al., "Switchable, Recyclable, and Time-Programmable Hydrogels via Counterion-Engineered Differential Metal-Ion Coordination," *Advanced Functional Materials* 36 (2025): 14481.

27. S. Xi, H. J. Zhang, X. Liu, et al., "Effect of Hydrogen Bonding Strength on the Structure and Properties of Phase-Separated Hydrogel From Gelatin," *Polymer* 316 (2025): 127870, https://doi.org/10.1016/j.polymer.2024.127870.

28. X. Hu, X. Tan, I. Ullah, et al., "Velcro-Inspired Poly(ethylene glycol) Gel (PEGgel) for Robust Interface Adhesion Between Hydrogel, Device, and Tissue," *ACS Nano* 19 (2025): 20128–20143, https://doi.org/10.1021/acsnano.5c04790.

29. L. Song, Z. Wang, S. Chen, Y. Shen, J. Yin, and R. Wang, "Phytic Acid-Induced Gradient Hydrogels for Highly Sensitive and Broad Range Pressure Sensing," *Advanced Materials* 37 (2025): 2417978, https://doi.org/10.1002/adma.202417978.

30. K. Chen, A. P. Rowley, J. D. Weiland, and M. S. Humayun, "Elastic Properties of Human Posterior Eye," *Journal of Biomedical Materials Research Part A* 102 (2014): 2001–2007.

31. Z. Fu, H. Liu, Q. Lyu, J. Dai, C. Ji, and Y. Tian, "Anti-Freeze Hydrogel-Based Sensors for Intelligent Wearable Human-Machine Interaction," *Chemical Engineering Journal* 481 (2024): 148526, https://doi.org/10.1016/j.cej.2024.148526.

32. H. Chen, Z. Zhao, R. Zhang, et al., "Adaptable Hydrogel With Strong Adhesion of Wet Tissue for Long-Term Protection of Periodontitis Wound," *Advanced Materials* 37 (2025): 2413373, https://doi.org/10.1002/adma.202413373.

33. P. Ma, W. Liang, R. Huang, et al., "Super-Structured Wet-Adhesive Hydrogel With Ultralow Swelling, Ultrahigh Burst Pressure Tolerance, and Anti-Postoperative Adhesion Properties for Tissue Adhesion," *Advanced Materials* 36 (2024): 2305400, https://doi.org/10.1002/adma.202305400.

34. H. J. Kee, E. J. Lee, J. C. Han, and C. Kee, "Ahmed Implant Coated With poly(2-methacryloyloxyethyl phosphorylcholine) Inhibits Foreign Body Reactions in Rabbit Eyes," *PLoS ONE* 16 (2021): 0252467, https://doi.org/10.1371/journal.pone.0252467.

35. C. Cai, W. Wang, J. Liang, et al., "MMP-2 Responsive Unidirectional Hydrogel-Electrospun Patch Loading TGF-β1 siRNA Polyplexes for Peritendinous Anti-Adhesion," *Advanced Functional Materials* 31 (2021): 2008364, https://doi.org/10.1002/adfm.202008364.

36. W. Chen, S. Sheng, K. Tan, et al., "Injectable Hydrogels for Bone Regeneration With Tunable Degradability via Peptide Chirality Modification," *Materials Horizons* 11 (2024): 4367–4377, https://doi.org/10.1039/D4MH00398E.

37. C. Cai, X. Zhang, Y. Li, et al., "Self-Healing Hydrogel Embodied With Macrophage-Regulation and Responsive-Gene-Silencing Properties for Synergistic Prevention of Peritendinous Adhesion," *Advanced Materials* 34 (2022): 2106564, https://doi.org/10.1002/adma.202106564.

38. P. I. Lee, "Kinetics of Drug Release From hydrogel Matrices," *Journal of Controlled Release* 2 (1985): 277–288, https://doi.org/10.1016/0168-3659(85)90051-3.

39. S. Tang, K. Feng, R. Yang, et al., "Multifunctional Adhesive Hydrogels: From Design to Biomedical Applications," *Advanced Healthcare Materials* 14 (2025): 2403734, https://doi.org/10.1002/adhm.202403734.

40. W. Zhang, B. Bao, F. Jiang, et al., "Promoting Oral Mucosal Wound Healing With a Hydrogel Adhesive Based on a Phototriggered S-Nitrosylation Coupling Reaction," *Advanced Materials* 33 (2021): 2105667.

41. G. Y. Han, J. Y. Park, T. H. Lee, M. B. Yi, and H. J. Kim, "Highly Resilient Dual-Crosslinked Hydrogel Adhesives Based on a Dopamine-Modified Crosslinker," *ACS Applied Materials & Interfaces* 14 (2022): 36304–36314, https://doi.org/10.1021/acsami.2c04791.

42. Y. Gong, C. Li, B. Zhu, et al., "Engineering Injectable Bioadhesives With Sealing and Anti-Fouling Properties for Postoperative Anti-Adhesion," *Chemical Engineering Journal* 500 (2024): 156747, https://doi.org/10.1016/j.cej.2024.156747.

43. C. Yu, M. Shi, S. He, et al., "Chronological Adhesive Cardiac Patch for Synchronous Mechanophysiological Monitoring and Electrocoupling Therapy," *Nature Communications* 14 (2023): 6226, https://doi.org/10.1038/s41467-023-42008-9.

44. J. Deng, H. Yuk, J. Wu, et al., "Electrical Bioadhesive Interface for Bioelectronics," *Nature Materials* 20 (2021): 229–236, https://doi.org/10.1038/s41563-020-00814-2.

45. Y. Chen, H. Tang, Y. Zhang, et al., "Multiplexed Self-Adaptable Janus Hydrogels Rescue Epithelial Malfunction to Promote Complete Trachea Repair," *Nature Communications* 16 (2025): 5734, https://doi.org/10.1038/s41467-025-61135-z.

46. Y. Lv, Y. Xu, S. Zhang, et al., "Rapidly Photocurable and Strongly Adhesive Hydrogel-Based Sealant With Good Procoagulant Activity for Lethal Hemorrhage Control," *Advanced Functional Materials* 35 (2025): 2501904, https://doi.org/10.1002/adfm.202501904.

47. F. Saeedinejad, F. Alipanah, S. Toro, et al., "In Situ-Formed Tissue-Adhesive Macroporous Scaffolds Enhance Cell Infiltration and Tissue Regeneration," *Acta Biomaterialia* 200 (2025): 358–377, https://doi.org/10.1016/j.actbio.2025.04.049.

48. Y. Quan, H. Shao, N. Wang, Z. Gao, and M. Jin, "Microenvironment-Sensitive Hydrogels as Promising Drug Delivery Systems for Co-Encapsulating Microbial Homeostasis Probiotics and Anti-Inflammatory Drugs to Treat Periodontitis," *Materials Today Bio* 32 (2025): 101711, https://doi.org/10.1016/j.mtbio.2025.101711.

49. P. Ramesh, R. Pena, J. M. Morrissey, et al., "Cryoelectrospun Elastin-Alginate Scaffolds as Potential Cell Delivery Vehicles for Mesenchymal Stromal Cell Therapy," *Scientific Reports* 15 (2025): 19847, https://doi.org/10.1038/s41598-025-03822-x.

50. Z. Dai, Y. Wang, N. Sun, and C. Zhang, "Characterizing Ligand-Receptor Interactions and Unveiling the Pro-Tumorigenic Role of CCL16-CCR1 Axis in the Microenvironment of Hepatocellular Carcinoma," *Frontiers in Immunology* 14 (2024): 1299953, https://doi.org/10.3389/fimmu.2023.1299953.

51. Q. Zhang, L. Shi, H. He, et al., "Down-Regulating Scar Formation by Microneedles Directly via a Mechanical Communication Pathway," *ACS Nano* 16 (2022): 10163–10178, https://doi.org/10.1021/acsnano.1c11016.

52. X. Liu, Y. Sun, J. Wang, et al., "A Tough, Antibacterial and Antioxidant Hydrogel Dressing Accelerates WoundHealing and Suppresses Hypertrophic Scar Formation in Infected Wounds," *Bioactive Materials* 34 (2024): 269–281, https://doi.org/10.1016/j.bioactmat.2023.12.019.

53. Y. Wang, X. Lu, J. Lu, P. Hernigou, and F. Jin, "The Role of Macrophage Polarization in Tendon Healing and Therapeutic Strategies: Insights From Animal Models," *Frontiers in Bioengineering and Biotechnology* 12 (2024): 1366398, https://doi.org/10.3389/fbioe.2024.1366398.

54. X. Liu, M. Wang, Y. Jiang, et al., "Magnetic Resonance Imaging Nanoprobe Quantifies Nitric Oxide for Evaluating M1/M2 Macrophage Polarization and Prognosis of Cancer Treatments," *ACS Nano* 17 (2023): 24854–24866, https://doi.org/10.1021/acsnano.3c05627.

55. R. Wang, B. Chen, H. Wei, et al., "Collecting and Deactivating TGF-β1 Hydrogel for Anti-Scarring Therapy in Post-Glaucoma Filtration Surgery," *Materials Today Bio* 14 (2022): 100260, https://doi.org/10.1016/j.mtbio.2022.100260.

56. A. P. Veith, K. Henderson, A. Spencer, A. D. Sligar, and A. B. Baker, "Therapeutic Strategies for Enhancing Angiogenesis in Wound Healing," *Advanced Drug Delivery Reviews* 146 (2019): 97–125, https://doi.org/10.1016/j.addr.2018.09.010.

57. F. Hu, G. Zheng, Y. Li, et al., "Injectable Metal-Free Carbon Dot-Integrated Hydrogel for Regulating Inflammation via Macrophage Metabolic Reprograming in Spinal Cord Injury Therapy," *ACS Nano* 20 (2026): 9603–9618, https://doi.org/10.1021/acsnano.5c13627.

58. X. Shi, Z. Lin, D. Xiao, et al., "Pathology-Responsive Light-Triggered Conjunctival Adhesive Implantable Hydrogels for Effective Anti-Scarring After Glaucoma Filtering Surgery," *Journal of Controlled Release* 392 (2026): 114677, https://doi.org/10.1016/j.jconrel.2026.114677.

59. T. Wang, W. Cao, X. Wang, et al., "Composite Synthetic Protein Hydrogel for Inhibition of Corneal Fibrosis and Treatment of Corneal Wounds," *International Journal of Biological Macromolecules* 307 (2025): 142013, https://doi.org/10.1016/j.ijbiomac.2025.142013.

60. H. M. Abdel-Mageed, N. Z. AbuelEzz, A. A. Ali, et al., "Newly Designed Curcumin-Loaded Hybrid Nanoparticles: A Multifunctional Strategy for Combating Oxidative Stress, Inflammation, and Infections to Accelerate Wound Healing and Tissue Regeneration," *BMC Biotechnology* 25 (2025): 49, https://doi.org/10.1186/s12896-025-00989-z.

61. Y. Lin, W. Luo, B. Jiang, et al., "The Effect of GelDex-S58 Hydrogel on Anti-Conjunctival Scarring After Glaucoma Filtration Surgery," *Iscience* 26 (2023): 107633, https://doi.org/10.1016/j.isci.2023.107633.

Supporting Information

Additional supporting information can be found online in the Supporting Information section.

Supporting File: adfm76484-sup-0001-SuppMat.docx.